

cuGUGA: Operator-Direct Graphical Unitary Group Approach Accelerated with CUDA

Zihan Pengmei

Department of Chemistry and James Franck Institute, University of Chicago, Chicago, Illinois 60637, United States

We present cuGUGA, an operator-direct graphical unitary group approach (GUGA) configuration interaction (CI) solver in a spin-adapted configuration state function (CSF) basis. Dynamic-programming walk counts provide constant-time CSF ranking/unranking, and pretabulated segment factors enable constant-time evaluation of coupling coefficients. Two-electron contributions are organized through an intermediate-weight formulation that separates sparse generator enumeration from integral contraction and supports both dense and density-fitted/Cholesky backends. We further map the same primitives to GPUs by implementing the irregular DRT traversal and accumulation in custom CUDA kernels while delegating contractions to CUDA libraries. The implementation reproduces reference energies at the 10^{-11} Eh level and matches CPU/GPU σ -vectors to 10^{-14} . On an RTX 4090, the GPU backend provides up to $\sim 10\times$ speedup over the CPU backend for smaller active spaces and multifold speedups on representative CASCI kernels. Speedup decreases as the active space grows because the workload becomes increasingly dominated by FP64 GEMM, which is not strongly accelerated on consumer GPUs. In addition, the cuGUGA CPU backend generally delivers $\gtrsim 2\times$ speedup over PySCF’s determinant backend and $\gtrsim 4\times$ speedup over PySCF’s CSF backend.

I. INTRODUCTION

Accurate electronic-structure predictions for strongly correlated molecules and materials with near-degenerate frontier orbitals often require multireference treatments. Complete active space self-consistent field (CASSCF) addresses strong correlation by solving the full configuration interaction (FCI) problem in a chosen active orbital subspace and remains a workhorse reference for post-CASSCF correlation methods.¹ In practice, each macro-iteration of orbital optimization requires repeated solutions of a large CI eigenproblem, most commonly with a Davidson-type iterative eigensolver.² The dominant cost is the repeated matrix–vector product (the “ σ -vector”), $\sigma = \mathbf{H}\mathbf{c}$, evaluated many times per root and per macro-iteration.

A standard strategy to reduce the CI dimension while enforcing spin purity is to work in a spin-adapted configuration state function (CSF) basis rather than in a Slater-determinant basis. In the graphical unitary group approach (GUGA), CSFs correspond to root-to-leaf walks on a layered directed acyclic graph (DAG, the Shavitt graph) encoded by a distinct row table (DRT).^{3–5} This representation enables systematic enumeration of CSFs and evaluation of Hamiltonian couplings through local “segment” rules for the action of spin-free generators.

Despite this structure, practical CI implementations often introduce determinant intermediates and/or large cached objects in the hot loop, which can mask the fine-grained sparsity of CSF couplings and complicate GPU execution. For example, OpenMolcas implements the RASSCF CI step using split-GUGA ideas but relies on determinant-based kernels in the innermost loops for Davidson σ -vector formation and reduced density matrices.^{6–8} Such designs are robust for CPU workflows, but they are not naturally aligned with a CSF-direct, graph-sparse formulation.

In this technical note, we introduce cuGUGA, an

operator-direct GUGA CI solver that cleanly separates (i) sparse coupling enumeration in the CSF basis via DRT traversal (“segment-walks”) and (ii) integral contraction backends used to form effective operator weights. We support both dense four-index integrals and density-fitted/Cholesky-factorized representations through a common intermediate-weight construction.^{9,10} Building on this hardware-agnostic formulation, we map the same primitives to GPUs by implementing the irregular DRT enumeration and accumulation in custom CUDA kernels while delegating dense/sparse contractions and Davidson subspace algebra to CUDA libraries.

The remainder of the note is organized as follows. Sec. II B introduces the DRT representation and the walk-count indexing used for CSF ranking/unranking. Sec. II C presents the segment-walk neighbor oracle and our lookup-table (LUT) strategy for constant-time evaluation of local segment factors. Sec. II D describes the operator-direct $\sigma = \mathbf{H}\mathbf{c}$ construction together with dense and DF/Cholesky integral backends. Sec. II E details the GPU mapping and the resulting end-to-end GPU-resident Davidson iteration.

II. METHODS

A. Overview: operator-direct CI in a GUGA CSF basis

We solve for low-lying eigenpairs of the active-space Hamiltonian in a spin-adapted CSF basis $\{|\Phi_j\rangle\}_{j=0}^{N_{\text{CSF}}-1}$. The iterative eigensolver (Davidson) requires repeated application of the Hamiltonian to one or more trial vectors,

$$\sigma = \mathbf{H}\mathbf{c}, \quad \sigma_i = \sum_{j=0}^{N_{\text{CSF}}-1} H_{ij} c_j. \quad (1)$$

TABLE I. Notations.

Symbol	Meaning	Notes / dimensions
n_{orb}	Number of active orbitals	Orbitals indexed by $p, q, r, s \in \{1, \dots, n_{\text{orb}}\}$
N_e	Number of active electrons	Fixed for the CI space
N_{CSF}	Number of CSFs in the target symmetry/spin sector	$N_{\text{CSF}} = W(v_{\text{root}})$
n_{pair}	Pair-space dimension	$n_{\text{pair}} = n_{\text{orb}}^2$ for ordered pairs (p, q)
n_{root}	Number of desired eigenpairs	Davidson roots
m	Davidson subspace dimension	Typically $m \ll N_{\text{CSF}}$
$ \Phi_j\rangle$	j th CSF basis function	CSF indices $i, j, \mu \in \{0, \dots, N_{\text{CSF}} - 1\}$
\mathbf{H}	CI Hamiltonian in CSF basis	Not explicitly formed
\mathbf{c}	CI coefficient vector	Trial vector in Davidson
σ	$\sigma = \mathbf{Hc}$	Dominant computational primitive
E_{pq}	Spin-free one-body generator	$E_{pq} = \sum_{\omega=\alpha, \beta} a_{p\omega}^\dagger a_{q\omega}$
$\mathcal{N}(j; pq)$	Neighbor set under E_{pq}	Indices i with $\langle \Phi_i E_{pq} \Phi_j \rangle \neq 0$
h_{pq}	One-electron integrals	Active-space one-electron Hamiltonian
$(pq rs)$	Two-electron repulsion integrals	Physicist's notation (may be permuted in contractions)
v_{pqrs}	Two-electron tensor consistent with chosen operator form	Used in $\sum_{pqrs} v_{pqrs} E_{pq} E_{rs}$
\mathcal{V}	Set of DRT nodes	Each node v corresponds to a prefix state
$v_{\text{root}}, v_{\text{leaf}}$	Root / leaf DRT nodes	Define target $(N_e, b_{\text{target}}, \Gamma_{\text{target}})$
$v \equiv (k, n_e, b, \Gamma)$	DRT node label	k layer, n_e electrons so far, b spin label, Γ symmetry
b	Integer spin-coupling label	Commonly $b = 2S$
Γ	(Optional) accumulated spatial symmetry label	Omitted if symmetry not enforced
\mathcal{D}	Step alphabet {E, U, L, D}	Empty / single-up / single-low / double
$d_k^{(j)}$	Step at orbital k for CSF j	Step sequence $\mathbf{d}^{(j)} = (d_1^{(j)}, \dots, d_{n_{\text{orb}}}^{(j)})$
$\chi(v, d)$	DRT transition map	$\chi : \mathcal{V} \times \mathcal{D} \rightarrow \mathcal{V} \cup \{\perp\}$
$W(v)$	Suffix walk count from node v	DP-computed number of root-to-leaf completions
$\Pi(v, d)$	Prefix sum for lexicographic offsets	$\Pi(v, d) = \sum_{d' \prec d} W(\chi(v, d'))$
$\rho(\mathbf{d})$	Lexicographic CSF rank	$\rho(\mathbf{d}) \in \{0, \dots, N_{\text{CSF}} - 1\}$
$R_j(t)$	Partial rank accumulator for ket j	$R_j(t) = \sum_{k=1}^t \Pi(v_{k-1}^{(j)}, d_k^{(j)})$
$n(d)$	Occupancy implied by a step	$n(\text{E}) = 0, n(\text{U}) = n(\text{L}) = 1, n(\text{D}) = 2$
$n_p(\Phi_j)$	Occupancy of orbital p in CSF j	Implied by $d_p^{(j)}$
$\mathcal{H}(j)$	"Hole" orbitals for ket j	$\{q n_q(\Phi_j) > 0\}$
$\mathcal{P}(j)$	"Particle" orbitals for ket j	$\{p n_p(\Phi_j) < 2\}$
$[p_<, p_>]$	Segment for E_{pq} action	$p_< = \min(p, q), p_> = \max(p, q)$
$\kappa(k; p, q)$	Segment position code	Encodes start/mid/end and direction
$S(\cdot)$	Local segment factor	Evaluated via pretabulated forms (LUT)
$M(\cdot), F[m, b]$	Case map and coefficient table	M selects analytic form; F tabulates values vs. b
ω	Segment-walk coefficient	$\omega = \langle \Phi_i E_{pq} \Phi_j \rangle$
$C_{\mu j}^{(rs)}$	Intermediate coefficients	$C_{\mu j}^{(rs)} = \langle \Phi_\mu E_{rs} \Phi_j \rangle$
$g_{pq}^{(\mu j)}$	Effective weights for applying E_{pq} to $ \Phi_\mu\rangle$	$g_{pq}^{(\mu j)} = \frac{1}{2} \sum_{rs} v_{pqrs} C_{\mu j}^{(rs)}$
$\alpha = (p, q), \beta = (r, s)$	Pair indices	Ordered pairs, $\alpha, \beta \in \{1, \dots, n_{\text{pair}}\}$
$V_{\alpha\beta}$	Dense pair-space matrix	$V_{\alpha\beta} = v_{pqrs}$
$B_{pq, L}$	DF/Cholesky factors	$v_{pqrs} \approx \sum_L B_{pq, L} B_{rs, L}$
N_L	Number of DF auxiliaries / Cholesky vectors	Determines factor rank

In a GUGA formulation, Hamiltonian matrix elements are evaluated operator-directly via spin-free generators⁴

$$E_{pq} = \sum_{\omega \in \{\alpha, \beta\}} a_{p\omega}^\dagger a_{q\omega}, \quad (2)$$

whose action on a CSF $|\Phi_j\rangle$ produces a sparse linear

combination of CSFs,

$$E_{pq} |\Phi_j\rangle = \sum_{i \in \mathcal{N}(j; pq)} \langle \Phi_i | E_{pq} | \Phi_j \rangle |\Phi_i\rangle. \quad (3)$$

Here $\mathcal{N}(j; pq)$ denotes the set of CSFs connected to $|\Phi_j\rangle$ by E_{pq} ; it is typically small and can be enumerated using the DRT representation of the CSF space (Sec. II B) and a DRT traversal routine called a *segment-walk* (Sec. II C).

Both the one- and two-electron parts of the active-

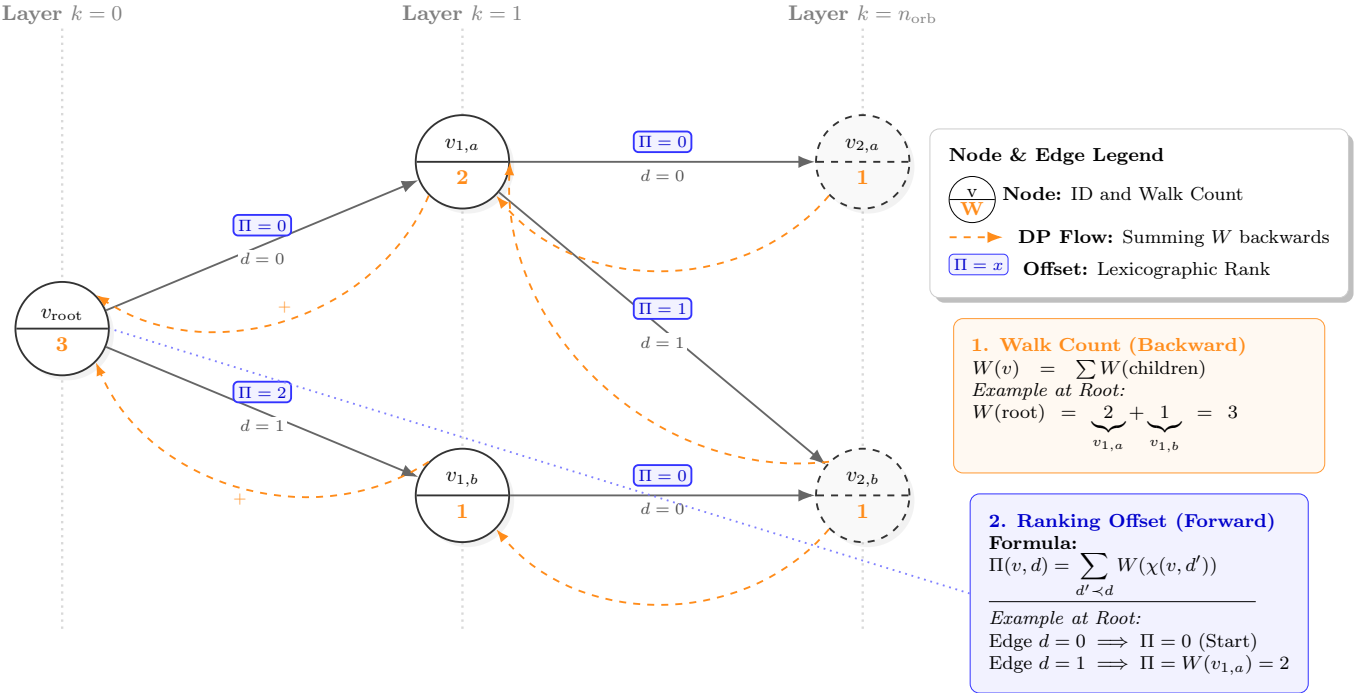


FIG. 1. **DRT graph parameters for CSF ranking.** Orange node labels show the suffix walk counts $W(v)$, computed via backward dynamic programming. Blue edge labels display the prefix sums $\Pi(v, d)$, which define the lexicographic offsets required for ranking and unranking CSFs.

space Hamiltonian can be written in terms of E_{pq} and products $E_{pq}E_{rs}$ (Sec. II D 2). The cuGUGA implementation computes contributions to σ by (i) enumerating connected CSFs and the associated coefficients induced by spin-free generators, and (ii) contracting these coefficients with the chosen integral representation (dense or density-fitted/Cholesky), without ever forming \mathbf{H} explicitly.

B. DRT representation of the CSF space and its construction

1. DRT as a layered directed acyclic graph (Shavitt graph)

A CSF can be represented as a root-to-leaf path on a layered DAG with layers corresponding to orbital positions $k = 0, 1, \dots, n_{\text{orb}}$ (the Shavitt graph / DRT representation).^{3–5} Each orbital transition on the path chooses one of four step types, which we store as integer codes:

- $d = 0$: E denotes an empty orbital (0 electrons),
- $d = 1$: U denotes a singly occupied orbital (1 electron) that raises the spin-coupling label,
- $d = 2$: L denotes a singly occupied orbital (1 electron) that lowers the spin-coupling label,
- $d = 3$: D denotes a doubly occupied orbital (2 electrons).

We denote the step alphabet by $\mathcal{D} = \{E, U, L, D\}$ and assume a fixed total order $E \prec U \prec L \prec D$ for lexicographic ranking. Each DRT node corresponds to a prefix state after processing the first k orbitals and is labeled by

$$v \equiv (k(v), n_e(v), b(v), \Gamma(v)), \quad (4)$$

where $n_e(v)$ denotes the number of electrons placed so far, $b(v)$ is an integer spin-coupling label (commonly $b = 2S$), and $\Gamma(v)$ optionally accumulates spatial symmetry.

We define the DRT via a transition map

$$\chi : \mathcal{V} \times \mathcal{D} \rightarrow \mathcal{V} \cup \{\perp\}, \quad (5)$$

where $\chi(v, d)$ returns the child node reached from node v by step d and $\chi(v, d) = \perp$ denotes a forbidden transition. We denote the root and leaf nodes by v_{root} and v_{leaf} , corresponding to the desired active-space quantum numbers (electron number, target spin label, and symmetry).

2. Walk counts, prefix sums, and CSF indexing

A central object is the suffix walk count

$$W(v) = \#\{\text{valid paths from node } v \text{ to } v_{\text{leaf}}\}, \quad (6)$$

which is computed by dynamic programming (DP) on the layered DAG. We also define the prefix-sum function

$$\Pi(v, d) = \sum_{d' \prec d} W(\chi(v, d')), \quad W(\perp) = 0, \quad (7)$$

which gives the lexicographic offset contributed by selecting step d at node v . For a root-to-leaf path $(v_0, d_1, v_1, \dots, d_{n_{\text{orb}}}, v_{n_{\text{orb}}})$ with $v_0 = v_{\text{root}}$ and $v_k = \chi(v_{k-1}, d_k)$, the corresponding CSF index (lexicographic rank) is

$$\rho(\mathbf{d}) = \sum_{k=1}^{n_{\text{orb}}} \Pi(v_{k-1}, d_k) \in \{0, \dots, N_{\text{CSF}} - 1\}, \quad (8)$$

and the total number of CSFs is $N_{\text{CSF}} = W(v_{\text{root}})$.

The DP construction of χ , W , and Π is summarized in Appendix Algorithm A1 and illustrated in Fig. 1. The inverse mapping (“unranking”) produces the step sequence $\mathbf{d}^{(j)} = (d_1^{(j)}, \dots, d_{n_{\text{orb}}}^{(j)})$ and corresponding node sequence $(v_0^{(j)}, \dots, v_{n_{\text{orb}}}^{(j)})$ for a given CSF index j (Appendix Algorithm A2; Fig. 2).

For later use in segment-walk indexing, we define the partial-rank accumulator for ket j :

$$R_j(t) \equiv \sum_{k=1}^t \Pi(v_{k-1}^{(j)}, d_k^{(j)}), \quad t = 0, 1, \dots, n_{\text{orb}}, \quad (9)$$

where $R_j(0) = 0$ and $R_j(n_{\text{orb}}) = j$.

C. Segment values and the segment-walk generator oracle

1. Occupancy feasibility and segment restriction

We define the orbital occupancy implied by a step as $n(\text{E}) = 0$, $n(\text{U}) = n(\text{L}) = 1$, and $n(\text{D}) = 2$. For a given CSF $|\Phi_j\rangle$ with step sequence $\mathbf{d}^{(j)}$, the occupancy of orbital p is $n_p(\Phi_j) = n(d_p^{(j)})$. For $p \neq q$, the spin-free generator E_{pq} transfers one electron from q to p (summed over spin). Therefore, a necessary feasibility condition for $E_{pq} |\Phi_j\rangle \neq 0$ is

$$n_q(\Phi_j) > 0 \quad \text{and} \quad n_p(\Phi_j) < 2. \quad (10)$$

Furthermore, only orbitals in the interval

$$[p_<, p_>] \equiv [\min(p, q), \max(p, q)] \quad (11)$$

may differ between the ket path and any connected bra path generated by E_{pq} ; this interval is called the *segment*. Denoting the ket node sequence by $(v_0^{(j)}, \dots, v_{n_{\text{orb}}}^{(j)})$, any valid segment replacement must start from the same boundary node $v_{p_<}^{(j)}$ and end at the same boundary node $v_{p_>+1}^{(j)}$.

2. Local segment factors and LUT evaluation

A segment-walk constructs admissible substitutions of steps along $k = p_<, \dots, p_>$ while enforcing DRT validity and the boundary constraint at $k = p_> + 1$. Each local substitution contributes a *segment factor* that depends on: (i) the segment position and direction (encoded by a discrete position code $\kappa(k; p, q)$), (ii) the proposed step \tilde{d}_k versus the ket step $d_k^{(j)}$, and (iii) the relevant spin label(s) on the DRT nodes involved. The total matrix element is a product of local factors along the segment.

To evaluate these factors in constant time, we introduce a two-level lookup: a finite case map $M(\kappa, \tilde{d}, d, \Delta b) \mapsto m$ selecting one of a finite family of coefficient forms $\{f_m(b)\}$, and a pretabulated array $F[m, b] = f_m(b)$ for $b = 0, \dots, b_{\text{max}}$, where $b_{\text{max}} = \max_{v \in \mathcal{V}} b(v)$. The local factor is then evaluated as $S = F[M(\cdot), b]$, where b is the chosen local spin label. Fig. 3 provides an overview of the two-level LUT, while Appendix Algorithm A3 gives the corresponding pseudocode.

3. Segment-walk neighbor oracle for $\langle \Phi_i | E_{pq} | \Phi_j \rangle$

During the segment-walk, the CSF index of a generated path can be assembled without reconstructing a full global rank. Let $\tilde{R}_{[p_<, p_>]}$ denote the accumulated rank contribution along a proposed segment walk, obtained by summing $\Pi(v, \tilde{d})$ for the visited segment nodes. For clarity, we define the prefix and suffix rank contributions of ket j relative to the segment endpoints as $R_{\text{pre}}^{(j)} \equiv R_j(p_< - 1)$ and $R_{\text{suf}}^{(j)} \equiv j - R_j(p_>)$. The resulting connected CSF index is

$$i = R_{\text{pre}}^{(j)} + \tilde{R}_{[p_<, p_>]} + R_{\text{suf}}^{(j)}, \quad (12)$$

where $R_j(\cdot)$ is defined in Eq. (9).

The full pseudocode for this boundary-constrained DFS is given in Appendix Algorithm A4. Fig. 4 provides a visual summary of the neighbor-oracle logic.

D. Operator-direct construction of $\sigma = \mathbf{H}\mathbf{c}$

Appendix Algorithms A1–A4 define a neighbor-oracle for the sparse action of E_{pq} in the CSF basis. For convenience we denote its output by

$$\mathcal{O}(p, q; j) \equiv \{(i, \omega) \mid \omega = \langle \Phi_i | E_{pq} | \Phi_j \rangle \neq 0\}, \quad (13)$$

that is, all connected bra indices i and their coupling coefficients for a fixed ket index j and orbital pair (p, q) . In this section, we use this oracle to build the operator-direct matrix–vector product $\sigma = \mathbf{H}\mathbf{c}$ required by Davidson iterations.

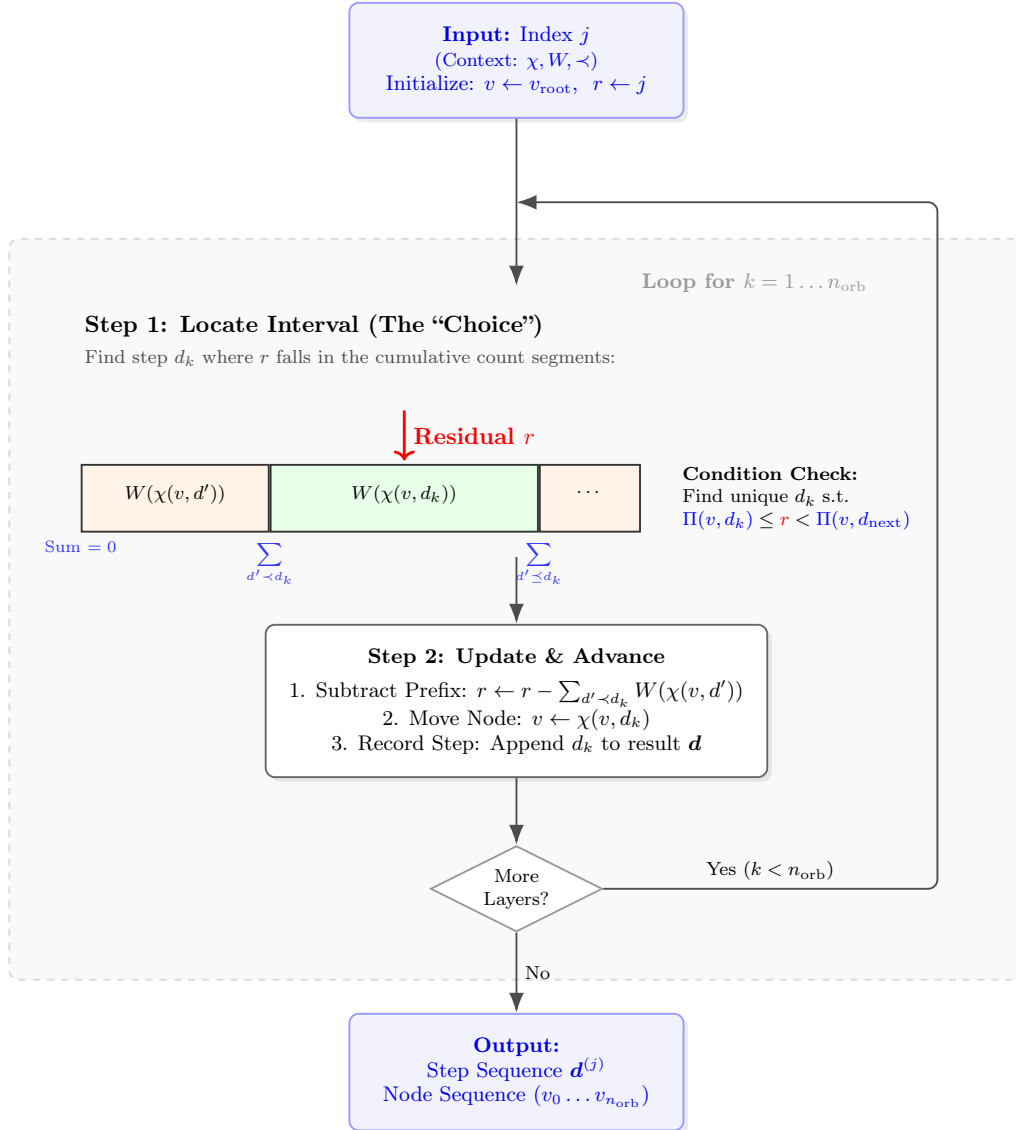


FIG. 2. Unranking (index-to-CSF) via walk counts. At each orbital layer, the residual index r selects the unique step d_k whose cumulative walk-count interval contains r , then updates r and advances to the next DRT node.

1. One-electron contribution

Using the step-to-occupancy mapping in Sec. II C 1, it is convenient to introduce the hole and particle index sets

$$\mathcal{H}(j) \equiv \{ q \mid n_q(\Phi_j) > 0 \}, \quad \mathcal{P}(j) \equiv \{ p \mid n_p(\Phi_j) < 2 \}, \quad (14)$$

since $E_{pq} |\Phi_j\rangle = 0$ unless $q \in \mathcal{H}(j)$ and $p \in \mathcal{P}(j)$.

The one-electron Hamiltonian in spin-free form is $\sum_{pq} h_{pq} E_{pq}$, and its contribution to the σ -vector is

$$\sigma_i^{(1)} = \sum_{j=0}^{N_{\text{CSF}}-1} c_j \sum_{p,q} h_{pq} \langle \Phi_i | E_{pq} | \Phi_j \rangle. \quad (15)$$

For $p \neq q$, the couplings $\langle \Phi_i | E_{pq} | \Phi_j \rangle$ are enumerated by

Algorithm A4. For $p = q$, E_{pp} is diagonal in this CSF basis and satisfies

$$E_{pp} |\Phi_j\rangle = n_p(\Phi_j) |\Phi_j\rangle, \quad (16)$$

so diagonal contributions can be accumulated without invoking the segment-walk oracle.

2. Two-electron contribution and spin-free generator factorization

We express the two-electron operator using the standard spin-free identity⁴

$$\sum_{\omega, \omega'} a_{p\omega}^\dagger a_{r\omega'}^\dagger a_{s\omega'} a_{q\omega} = E_{pq} E_{rs} - \delta_{qr} E_{ps}. \quad (17)$$

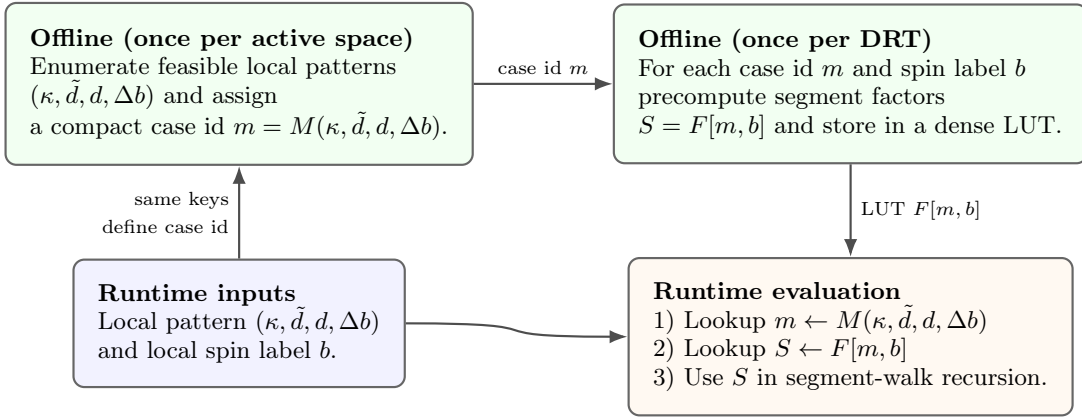


FIG. 3. Two-level lookup-table (LUT) strategy for constant-time evaluation of segment factors. A finite mapping assigns each feasible local pattern $(\kappa, \tilde{d}, d, \Delta b)$ a compact case id m , and a dense table $F[m, b]$ stores the corresponding segment factor for each allowed spin label b .

Accordingly, we write the two-electron part in the generator product form

$$\hat{V} = \frac{1}{2} \sum_{pqrs} v_{pqrs} (E_{pq} E_{rs} - \delta_{qr} E_{ps}), \quad (18)$$

where v_{pqrs} denotes a fixed index ordering of the two-electron integrals compatible with Eq. (18). (Concretely, v_{pqrs} is a permutation of the conventional tensor $(pq|rs)$; our implementation uses an ordering in which the outer indices align with the generator product $E_{pq} E_{rs}$.) The contraction term can be absorbed into an *effective* one-electron integral,

$$h_{ps}^{\text{eff}} \equiv h_{ps} - \frac{1}{2} \sum_q v_{pqqs}, \quad (19)$$

so the Hamiltonian can be written as

$$\mathbf{H} = \sum_{pq} h_{pq}^{\text{eff}} E_{pq} + \frac{1}{2} \sum_{pqrs} v_{pqrs} E_{pq} E_{rs}. \quad (20)$$

With this representation, both the one-electron and two-electron contributions reduce to applications of the generator oracle. For completeness, Appendix Algorithm A5 provides full pseudocode for the operator-direct $\sigma = \mathbf{H}c$ build.

3. Two-electron σ -vector via intermediate weights

We evaluate the two-electron contribution in Eq. (20) using an intermediate-weight decomposition. For a fixed source CSF $|\Phi_j\rangle$ and an operator E_{rs} , define the intermediate expansion

$$E_{rs} |\Phi_j\rangle = \sum_{\mu \in \mathcal{N}(j; rs)} C_{\mu j}^{(rs)} |\Phi_\mu\rangle, \quad C_{\mu j}^{(rs)} \equiv \langle \Phi_\mu | E_{rs} | \Phi_j \rangle. \quad (21)$$

For each resulting intermediate ket index μ , we define an effective weight tensor

$$g_{pq}^{(\mu j)} \equiv \frac{1}{2} \sum_{rs} v_{pqrs} C_{\mu j}^{(rs)}. \quad (22)$$

Then the two-electron action on $|\Phi_j\rangle$ can be written as

$$\frac{1}{2} \sum_{pqrs} v_{pqrs} E_{pq} E_{rs} |\Phi_j\rangle = \sum_{\mu} \sum_{pq} g_{pq}^{(\mu j)} E_{pq} |\Phi_\mu\rangle, \quad (23)$$

and the corresponding σ -vector contribution is

$$\sigma_i^{(2)} = \sum_{j=0}^{N_{\text{CSF}}-1} c_j \sum_{\mu} \sum_{pq} g_{pq}^{(\mu j)} \langle \Phi_\mu | E_{pq} | \Phi_\mu \rangle. \quad (24)$$

This decomposition separates the computation into two conceptually distinct stages: (i) *enumeration* of sparse coefficients $C_{\mu j}^{(rs)}$ using Algorithm A4, and (ii) *integral contraction* to form $g_{pq}^{(\mu j)}$ using either a dense or density-fitted/Cholesky backend (Sec. II D 4).

4. Integral backends: dense and density fitting / Cholesky

Let $\alpha = (p, q)$ and $\beta = (r, s)$ denote ordered pair indices, with $\alpha, \beta \in \{1, \dots, n_{\text{pair}}\}$ and $n_{\text{pair}} = n_{\text{orb}}^2$. For each task indexed by (μ, j) , define a (typically sparse) pair-space coefficient vector

$$(\mathbf{C}^{(\mu j)})_\beta \equiv C_{\mu j}^{(rs)}. \quad (25)$$

a. *Dense backend.* Define a dense pair-space matrix $\mathbf{V}^{(2e)} \in \mathbb{R}^{n_{\text{pair}} \times n_{\text{pair}}}$ by

$$V_{\alpha\beta} \equiv v_{pqrs}. \quad (26)$$

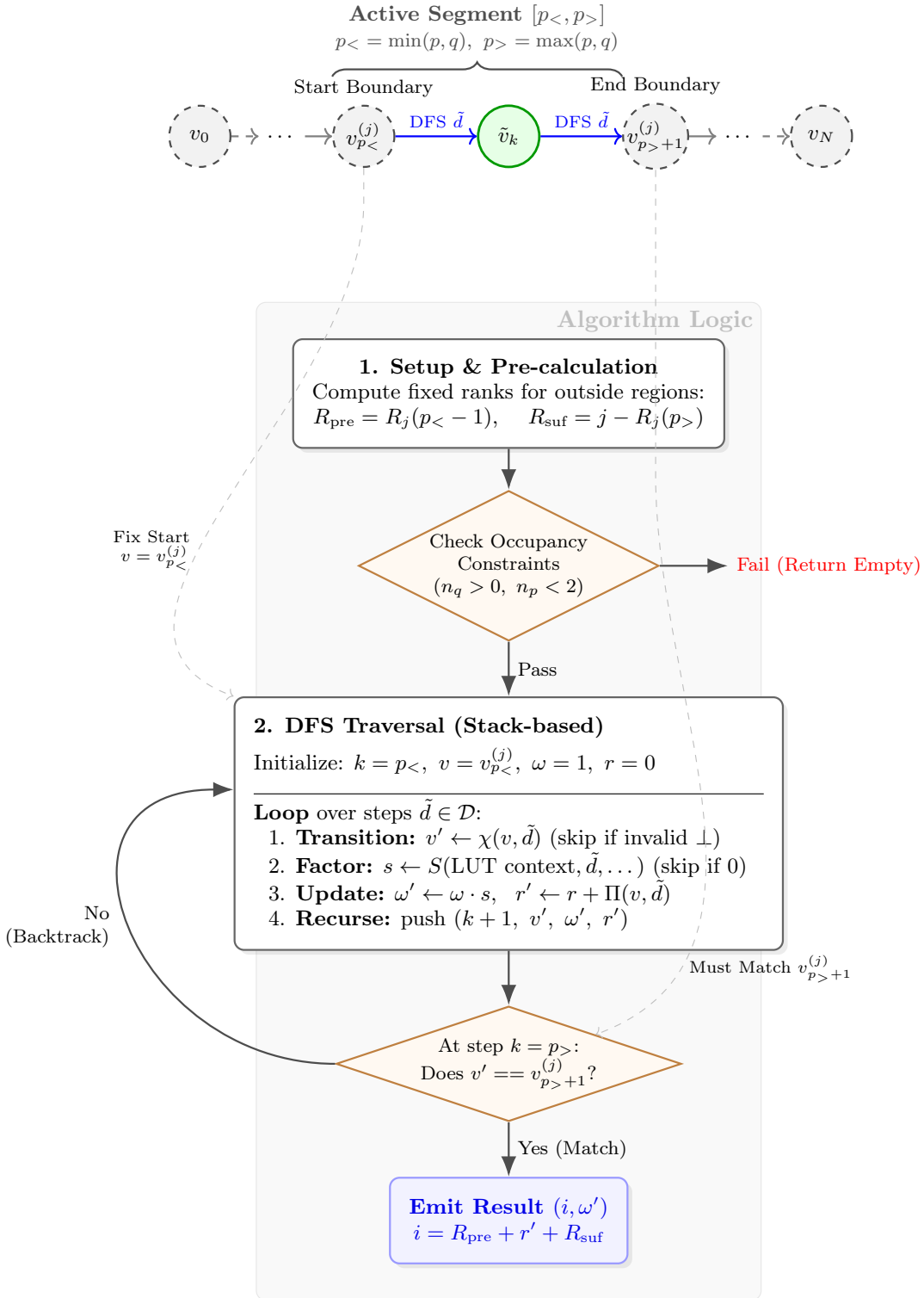


FIG. 4. Segment-walk neighbor oracle. The active segment $[p_<, p_>]$ (with $p_< = \min(p, q)$ and $p_> = \max(p, q)$) is explored by a boundary-constrained DFS between fixed prefix/suffix nodes of the ket CSF. Each valid path produces a connected bra index i and a coupling coefficient $\omega = \langle \Phi_i | E_{pq} | \Phi_j \rangle$.

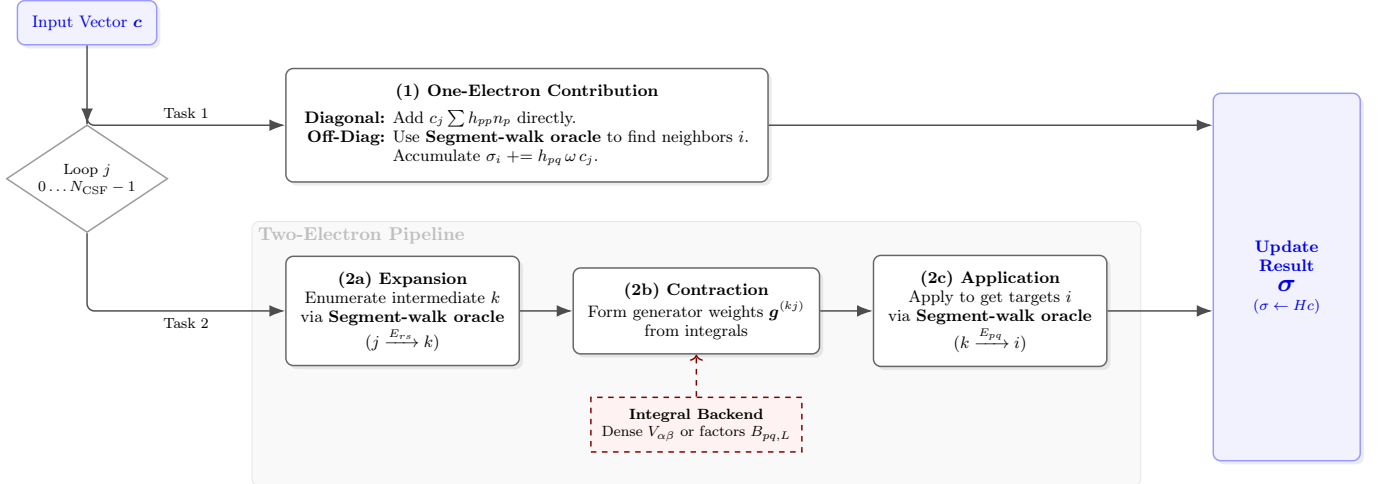


FIG. 5. Operator-direct $\sigma = \mathbf{H}\mathbf{c}$ build. One-electron contributions are accumulated directly (diagonal) or via segment-walk enumeration (off-diagonal). Two-electron contributions follow an expand–contract–apply pipeline that isolates integral contractions (dense or DF/Cholesky) from CSF coupling enumeration.

Then the weights in Eq. (22) are computed as

$$(\mathbf{g}^{(\mu j)})_\alpha = \frac{1}{2} \sum_\beta V_{\alpha\beta} (\mathbf{C}^{(\mu j)})_\beta. \quad (27)$$

$$\mathbf{g}^{(\mu j)} = \frac{1}{2} \mathbf{V}^{(2e)} \mathbf{C}^{(\mu j)}. \quad (28)$$

In practice, multiple (μ, j) tasks are processed in blocks, and the corresponding pair-space vectors are batched to enable matrix–matrix contractions.

b. *DF/Cholesky backend.* Assume a factorization^{9,10}

$$v_{pqrs} \approx \sum_{L=1}^{N_L} B_{pq,L} B_{rs,L}, \quad (29)$$

where L indexes auxiliary functions (or Cholesky vectors). For each (μ, j) task we compute

$$W_L^{(\mu j)} = \sum_{rs} B_{rs,L} C_{\mu j}^{(rs)}, \quad g_{pq}^{(\mu j)} = \frac{1}{2} \sum_L B_{pq,L} W_L^{(\mu j)}. \quad (30)$$

For a batch of tasks stacked as rows of a matrix \mathbf{C} , Eq. (30) becomes

$$\mathbf{W} = \mathbf{C}\mathbf{B}, \quad \mathbf{g} = \frac{1}{2} \mathbf{W}\mathbf{B}^\top, \quad (31)$$

where $\mathbf{B} \in \mathbb{R}^{n_{\text{pair}} \times N_L}$. This representation is particularly suitable for GPUs because it reduces the dominant contraction to sparse/dense and dense/dense matrix multiplications (Sec. II E).

E. GPU realization and CUDA-accelerated backends

The mathematical formulation of the solver is hardware-agnostic. However, directly porting a classical GUGA/CSF implementation to GPUs is challenging because legacy implementations often rely on pointer-heavy graph traversals, recursion, highly branch-dependent coefficient evaluation, and fine-grained irregular updates, all of which map poorly to SIMD execution. To enable efficient GPU parallelism, cuGUGA reorganizes the hot-path operations in $\sigma = \mathbf{H}\mathbf{c}$ into three stages:

$$\sigma = \underbrace{\text{Enumerate}}_{\text{custom CUDA}} + \underbrace{\text{Contract}}_{\text{cuBLAS / cuSPARSE}} + \underbrace{\text{Apply \& Accumulate}}_{\text{custom CUDA}}. \quad (32)$$

and keeps all solver data resident on the device across Davidson iterations.

1. GPU-enabling reformulation of GUGA primitives

The following changes are critical for GPU execution:

a. *Flattened DRT tables.* The DRT transition map $\chi(v, d)$ and prefix sums $\Pi(v, d)$ are stored as dense, contiguous device arrays indexed by (v, d) , eliminating pointer chasing and enabling coalesced memory access. The per-node spin label $b(v)$ and any auxiliary metadata required by segment factors are stored as compact device arrays.

b. *Table-driven segment factors.* Local segment factors are evaluated by a two-level lookup (Algorithm A3), replacing branch-heavy case logic with integer indexing into pretabulated coefficients. On GPUs this reduces warp divergence and avoids repeated expensive operations (e.g.,

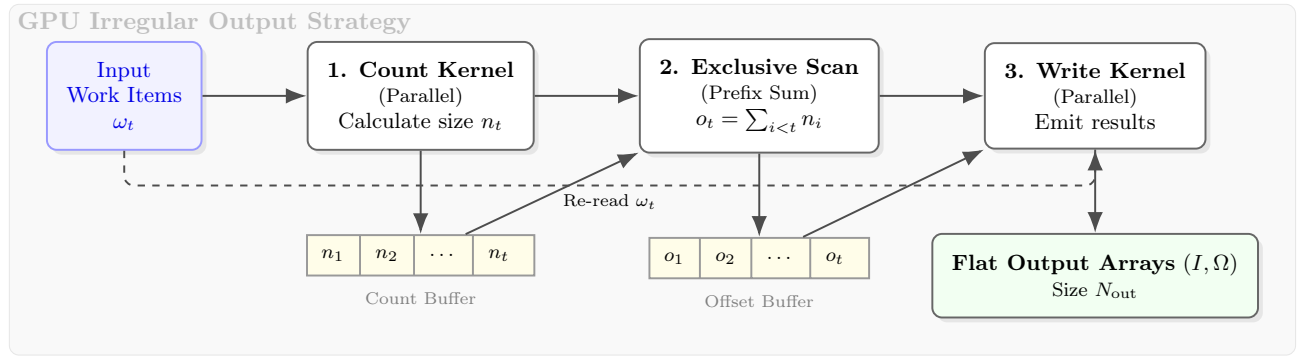


FIG. 6. GPU count–scan–write for irregular outputs. A first pass counts per-work-item output sizes, an exclusive prefix scan computes write offsets, and a second pass emits data into contiguous output buffers.

square roots).

c. *Batching and block-Davidson matvecs.* We apply \mathbf{H} to a *block* of vectors, $\mathbf{V} \in \mathbb{R}^{N_{\text{CSF}} \times m}$, rather than one vector at a time whenever possible. This enables the two-electron contraction stage to be expressed predominantly as GEMM/SpMM operations (high arithmetic intensity) rather than a large number of GEMV/SpMV calls.

d. *Count–scan–write enumeration for variable output size.* Because segment-walk enumeration produces a variable number of neighbors for each work item (p, q, j) , we cannot predict memory requirements in advance. To avoid the performance penalty of dynamic allocation during kernel execution, we employ a standard count–scan–write strategy. This involves: (i) a counting pass to compute the number of outputs, (ii) an exclusive scan to produce write offsets, and (iii) a write pass to emit (index, value) pairs into contiguous buffers.

2. Device-resident data and precision

The following objects are transferred once and kept resident on the GPU: (i) DRT tables χ , Π , and node labels $b(v)$; (ii) CSF path data (step sequences $\mathbf{d}^{(j)}$ and optional node sequences $(v_k^{(j)})$); (iii) segment-factor lookup tables $M(\cdot)$ and $F[m, b]$ (Algorithm A3); (iv) integrals in either dense pair-space form (Eq. (27)) or DF/Cholesky factors (Eq. (29)); and (v) Davidson workspaces $\mathbf{V}, \mathbf{W}, \mathbf{R}$ and diagonal H_{diag} . Unless otherwise stated, contractions and eigenvalue updates are performed in double precision.

3. Batched segment-walk enumeration on GPU

We treat a generator-application request as a work item $\omega \equiv (p, q, j)$. For each work item we need to evaluate the neighbor-oracle output set $\mathcal{O}(p, q; j)$ defined in Eq. (13). To handle the variable output size $|\mathcal{O}(p, q; j)|$ efficiently on GPUs, we employ a count–scan–write pipeline. Fig. 6 illustrates this strategy, and Appendix Algorithm A7 provides pseudocode. Occupancy feasibility constraints

(Eq. (10) and Eq. (14)) are applied before invoking the segment-walk to prune zero work.

4. Two-electron contraction on GPU: dense and DF/Cholesky backends

The intermediate-weight formulation (Eqs. (21)–(22)) produces a set of tasks indexed by (μ, j) , each associated with a sparse pair-space coefficient vector $\mathbf{C}^{(\mu j)}$ (Eq. (25)). Let n_{task} be the number of such tasks in a batch. We store the batch as a sparse matrix $\mathbf{C} \in \mathbb{R}^{n_{\text{task}} \times n_{\text{pair}}}$, typically in CSR format (row pointers, column indices, values).

a. *Dense backend.* When the dense pair-space matrix $\mathbf{V}^{(2e)}$ (Eq. (26)) fits in device memory and reuse across many Davidson iterations amortizes its storage, we compute

$$\mathbf{g} = \frac{1}{2} \mathbf{C} (\mathbf{V}^{(2e)})^T,$$

using cuBLAS GEMM (or GEMV if the block size is one). This is advantageous only for relatively small n_{orb} .

b. *DF/Cholesky backend.* For larger active spaces, the DF/Cholesky factorization $v_{pqrs} \approx \sum_L B_{pq,L} B_{rs,L}$ (Eq. (29)) is preferred. For a batch, Eq. (31) becomes

$$\mathbf{W} = \mathbf{C} \mathbf{B}, \quad \mathbf{g} = \frac{1}{2} \mathbf{W} \mathbf{B}^T.$$

We compute $\mathbf{W} = \mathbf{C} \mathbf{B}$ using cuSPARSE SpMM (CSR \times dense), followed by $\mathbf{g} = \frac{1}{2} \mathbf{W} \mathbf{B}^T$ using cuBLAS GEMM. The second GEMM is typically the dominant floating-point kernel and achieves high utilization when n_{task} is large.

After forming weights $g_{pq}^{(\mu j)}$, we apply weighted generators to each intermediate ket $|\Phi_\mu\rangle$ and accumulate into σ (Eq. (24)). This stage is again expressed in terms of segment-walk enumeration (Algorithm A4) and is implemented using custom CUDA kernels: each thread block (or cooperative group) processes one or a small number of intermediate kets μ , iterates over relevant (p, q) tiles,

enumerates neighbors $(i, \Omega_{i\mu}^{(pq)})$, and performs

$$\sigma_i += c_j g_{pq}^{(\mu j)} \Omega_{i\mu}^{(pq)}.$$

Because many tasks contribute to the same σ_i , the GPU implementation uses atomic accumulation in global memory. If strict bitwise reproducibility is required, an alternative deterministic mode writes contributions as a stream of $(i, \Delta\sigma_i)$ pairs and performs a reduce-by-key operation; this trades additional sorting/reduction overhead for deterministic summation order.

F. Implementation details and numerical settings

We use double precision (FP64) for CI vectors, segment factors, and all reported contractions. The CUDA dense-integral backend performs the dominant pair-space contractions with cuBLAS GEMM routines and keeps all Davidson vectors and intermediates resident on device during the iterative solve. To bound temporary memory for large CSF spaces, the CUDA backend processes the ket index j in tiles and allocates intermediate buffers according to a user-configurable workspace cap. Unless otherwise stated, no screening of Hamiltonian contributions is performed beyond the intrinsic sparsity of the E_{pq} neighbor enumerator (segment walk).

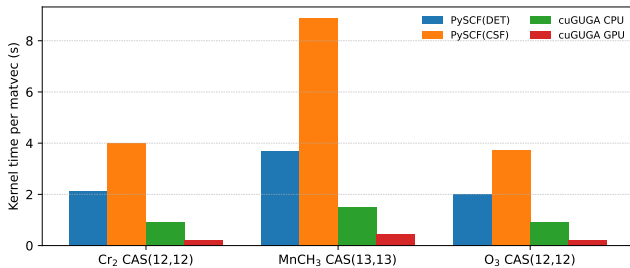


FIG. 7. CASCI kernel timings for three representative systems (fixed Davidson budget; mean over three repeats). The GPU bar corresponds to the cuGUGA backend on an RTX 4090.

G. Computational details

All benchmarks reported in Sec. III were run on an Intel Core i7-14700K CPU (14 cores / 28 threads) and an NVIDIA GeForce RTX 4090 GPU (24 GB VRAM), with NVIDIA driver 591.59 and CUDA 13.1. The software environment is Python 3.10.13, PySCF (PySCF-forge)^{11,12}, CuPy 13.6.0, and NumPy 2.2.6. Unless otherwise noted, CPU runs use all available logical CPUs (OpenBLAS and OpenMP set to 28 threads) without CPU pinning. For the “kernel” timing benchmarks we use a fixed Davidson budget of 5 iterations with a maximum subspace size of 8; reported times are mean wall times over three repeats after

TABLE II. Converged CASCI energies for O₃ in CAS(12,12) comparing PySCF and cuGUGA solvers. ΔE is reported relative to the PySCF determinant (DET) solver.

Solver	Backend	E (Eh)	ΔE (Eh)
PySCF	DET	-224.6516842783717	0
PySCF	CSF	-224.6516842783705	1.194×10^{-12}
cuGUGA	CPU	-224.6516842783876	-1.586×10^{-11}
cuGUGA	CUDA	-224.6516842783876	-1.589×10^{-11}

TABLE III. Cross-code CASSCF energy comparison for ethylene (6-31G*, CAS(2,2)). PySCF and cuGUGA share the same one- and two-electron integrals; Columbus and OpenMolcas energies are taken from their respective outputs. ΔE is relative to PySCF(DET).

Code	Backend	E (Eh)	ΔE (Eh)
PySCF	DET	-77.870218781788	0
cuGUGA	CPU	-77.870218781467	3.211×10^{-10}
cuGUGA	GPU	-77.870218781769	1.917×10^{-11}
Columbus	MCSCF	-77.870218782000	-2.121×10^{-10}
OpenMolcas	RASSCF	-77.87021875	3.179×10^{-8}

one warm-up run. We reuse O₃, MnCH₃, and Cr₂ molecular orbitals from an earlier work for benchmarking¹³.

III. RESULTS

A. Correctness: energies, cross-code validation, and σ agreement

Table II compares converged CASCI energies for O₃ in CAS(12,12) obtained from the PySCF determinant solver, PySCF’s CSF solver, and cuGUGA using both the CPU contraction backend and the CUDA dense-integral backend. All solvers agree to within $\sim 10^{-11}$ Eh, consistent with minor differences in Davidson termination and floating-point reduction order.

To validate cuGUGA against independent codes, Table III reports a cross-code CASSCF energy comparison for ethylene (6-31G*, CAS(2,2)). PySCF and cuGUGA share the same integrals and SCF reference, while Columbus and OpenMolcas are run externally.^{8,11,14} The cuGUGA GPU backend matches PySCF(DET) at the 10^{-11} Eh level; Columbus matches at $\sim 10^{-10}$ Eh. The larger apparent OpenMolcas deviation reflects the limited precision of the parsed OpenMolcas output in this benchmark set.

Beyond total energies, we directly compared $\sigma = \mathbf{H}\mathbf{c}$ produced by the CPU and GPU backends for two random CI vectors in O₃ / CAS(12,12). The maximum entrywise difference is 1.8×10^{-14} and the maximum relative ℓ_2 error is 1.3×10^{-14} . We also repeated a full CASCI solve three times to quantify run-to-run dispersion of the GPU path; the maximum observed energy deviation from the mean is 5.7×10^{-14} Eh. A compact summary of these diagnostics is given in Table IV.

TABLE IV. σ -vector agreement and run-to-run dispersion diagnostics for O_3 CAS(12,12). CPU vs GPU σ comparisons use two random CI vectors.

Metric	Value
max entrywise $ \Delta\sigma $ (CPU vs GPU)	1.751×10^{-14}
max relative ℓ_2 error (CPU vs GPU)	1.301×10^{-14}
max run-to-run $ \Delta E $ (GPU, 3 repeats)	5.684×10^{-14}
max run-to-run $ \Delta\sigma $ (GPU, 3 repeats)	5.551×10^{-16}

B. Performance: CPU baselines and GPU acceleration

Table V summarizes representative CASCI kernel timings for three test cases. On CPU, cuGUGA is consistently faster than the PySCF determinant solver by $\approx 2.2\times$ in these examples, and substantially faster than the PySCF CSF solver. Relative to the cuGUGA CPU backend, the CUDA dense-integral backend provides an additional $3.4\text{--}4.1\times$ kernel speedup on the RTX 4090. Notably, the speedup is largest for smaller active spaces: in the active-space sweeps of Fig. 9, the GPU backend reaches up to a $9.56\times$ speedup over the cuGUGA CPU backend ($MnCH_3$, CAS(11,13)), i.e., approximately $10\times$. Combining this with the typical $\sim 2\text{--}2.5\times$ advantage of cuGUGA CPU over PySCF(DET) in Table V suggests that, in this regime, overall speedups can exceed $20\times$ relative to PySCF(DET) and $40\times$ relative to PySCF(CSF). Fig. 7 visualizes these timings.

For O_3 /CAS(12,12) we also break down the σ -vector (matvec) stage into major components. Fig. 8 shows that, in the CPU backend, the apply/scatter phase dominates, whereas the GPU backend reduces apply/scatter dramatically and shifts the dominant cost toward the dense FP64 contraction (GEMM). In this benchmark, apply/scatter decreases from 0.316 s to 0.0138 s per matvec ($\sim 23\times$), and weight construction decreases from 0.0946 s to 0.0459 s ($\sim 2.1\times$). By contrast, the FP64 GEMM time changes only modestly (0.146 s \rightarrow 0.127 s, $\sim 1.15\times$). This asymmetry is consistent with the limited FP64 throughput of consumer GPUs: for AD102 (RTX 4090), the FP64 TFLOP rate is only 1/64 of the FP32 TFLOP rate, corresponding to ~ 1.3 TFLOPS peak FP64 on this device. As active spaces grow, the matvec becomes increasingly GEMM-dominated, so the overall GPU speedup decreases on the RTX 4090. We expect the GEMM component (and thus the end-to-end speedup trend) to improve substantially on data-center GPUs with far higher FP64 capability (Table VII).

Table VI reports the end-to-end Davidson timing decomposition for the same O_3 /CAS(12,12) benchmark. In this regime, the overall iteration time tracks the hop/matvec time closely; orthogonalization and subspace updates remain a small fraction of the total.

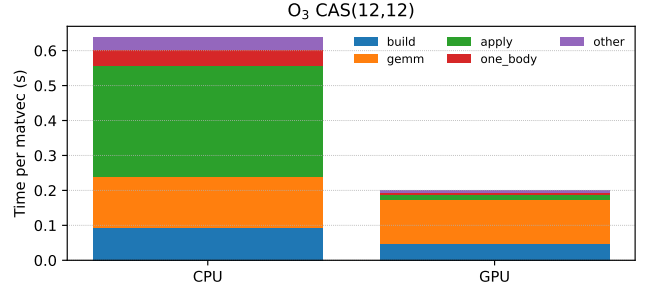


FIG. 8. Matvec (hop) timing breakdown for O_3 CAS(12,12) in the fixed-budget benchmark, comparing the cuGUGA CPU `contract` backend and the cuGUGA GPU backend. Bars are stacked by major phases.

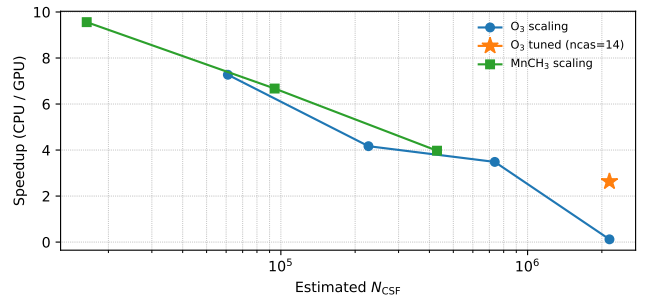


FIG. 9. Speedup of the cuGUGA GPU backend relative to the cuGUGA CPU backend as a function of the estimated CSF dimension. The starred point corresponds to a tuned O_3 CAS(14,12) run with capped workspace and FP64 GEMM settings.

C. Scaling with active-space size

Fig. 9 reports the GPU speedup of the cuGUGA dense-integral backend relative to the cuGUGA CPU backend for active-space sweeps in O_3 and $MnCH_3$. For both systems, the speedup decreases as the CSF dimension grows, with the largest accelerations observed in the small-active-space regime. Two effects contribute to this trend. First, as the active space increases, the matvec becomes increasingly dominated by dense FP64 contractions (GEMM), while the apply stage, where the GPU backend offers its strongest reduction (Fig. 8) becomes a smaller fraction of the total. On the RTX 4090, FP64 throughput is comparatively low (Table VII), limiting GEMM acceleration and thus reducing the overall speedup at large active spaces. Second, at the largest active spaces, performance becomes sensitive to workspace and buffering choices. The default O_3 CAS(14,12) point is pathological due to conservative workspace sizing; a tuned run with explicit buffering and FP64 GEMM settings restores a $2.6\times$ speedup at $N_{CSF} \approx 2.1 \times 10^6$. We are actively working on further workspace optimizations (e.g., more aggressive reuse of temporary buffers and adaptive tiling) to improve the

TABLE V. Representative CASCI kernel timings (seconds) for three systems. Unless otherwise noted, timings are mean wall times over three repeats (one warm-up excluded) with a fixed Davidson budget of 5 iterations and a maximum subspace size of 8. CPU baselines use all 28 logical CPUs; GPU timings use an RTX 4090. The final column reports the CPU/GPU wall-time ratio (values > 1 indicate the GPU is faster).

Case	CAS	N_{CSF}	PySCF(det)	PySCF(CSF)	cuGUGA CPU	cuGUGA GPU	CPU/GPU
O ₃	(12,12)	226 512	2.012	3.722	0.911	0.223	4.09
MnCH ₃	(13,13)	429 429	3.697	8.876	1.514	0.445	3.40
Cr ₂	(12,12)	226 512	2.110	4.011	0.911	0.223	4.09

TABLE VI. End-to-end Davidson timing breakdown for O₃ CAS(12,12) under the fixed-budget benchmark (5 iterations). “hop” denotes the $\mathbf{H}\mathbf{V}$ (matvec) stage.

Path	Total (s)	hop (s)	orth (s)	subspace (s)
cuGUGA CPU	0.682	0.640	0.0083	0.0302
cuGUGA GPU	0.219	0.203	0.0028	0.0044

TABLE VII. Peak dense FP64 throughput of the RTX 4090 used in this work compared to representative data-center GPUs. RTX 4090 FP64 is computed from the FP32 peak and the documented FP64 rate (1/64 of FP32).

GPU	Peak FP64 (TFLOPS)
GeForce RTX 4090	1.3
NVIDIA A100 (SXM)	9.7
NVIDIA H100 (SXM)	34
NVIDIA HGX B100 (per GPU)	30
NVIDIA HGX B200 (per GPU)	40

large-active-space regime.

IV. RELATION TO EXISTING IMPLEMENTATIONS

OpenMolcas provides widely used multiconfigurational workflows and supports GUGA-related machinery.⁸ The OpenMolcas RASSCF program is based on the split-GUGA formalism⁶ but uses determinant-based CI algorithms, performing CSF \rightarrow determinant transformations in the innermost loops required to evaluate Davidson σ vectors and reduced density matrices.⁷ In contrast, cuGUGA keeps the σ build CSF-direct and exposes dense pair-space contractions that map naturally to GPUs.

PySCF provides efficient determinant-based CASCI/-CASSCF drivers and FCI kernels in the `pyscf.mcscf` and `pyscf.fci` modules.¹¹ Determinant representations remain the most practical choice for many active-space calculations; cuGUGA instead targets cases where spin adaptation and CSF-direct sparsity are central and where GPU acceleration of the CI step is desired. The COLUMBUS program system contains mature GUGA-based CI and MRCl implementations and highly optimized parallel CPU algorithms for large configuration spaces.¹⁴ The differences to cuGUGA are primarily architectural: a GPU-oriented data layout and an explicit separation between sparse CSF enumeration and dense pair-space

contractions.

V. DATA AVAILABILITY

The cuGUGA source package and scripts to reproduce the benchmarks will be made publicly available upon publication. Data generated in this work are available from the corresponding author upon reasonable request.

VI. ACKNOWLEDGMENTS

This note reports work conducted by Z. P. as independent research. Parts of the software engineering and implementation were assisted by an LLM-based coding agent, OpenAI Codex¹⁵. OpenAI ChatGPT¹⁶ is used to enhance description clarity and notation checking. Z. P. thanks Dayou Zhang for providing molecular orbitals used for benchmarking.

- ¹B. O. Roos, P. R. Taylor, and P. E. M. Siegbahn, “A complete active space scf method (casscf) using a density matrix formulated super-ci approach,” *Chemical Physics* **48**, 157–173 (1980).
- ²E. R. Davidson, “The iterative calculation of a few of the lowest eigenvalues and corresponding eigenvectors of large real-symmetric matrices,” *Journal of Computational Physics* **17**, 87–94 (1975).
- ³I. Shavitt, “Graph theoretical concepts for the unitary group approach to the many-electron correlation problem,” *International Journal of Quantum Chemistry* **12**, 131–148 (1977).
- ⁴I. Shavitt, “Matrix element evaluation in the unitary group approach to the electron correlation problem,” *International Journal of Quantum Chemistry* **14**, 5–32 (1978).
- ⁵J. Paldus, “Relation of gelfand and weyl tableau formulations of the unitary-group approach to the many-electron correlation problem,” *Physical Review A* **14**, 1620 (1976).
- ⁶P.-A. Malmqvist, A. Rendell, and B. O. Roos, “The restricted active space self-consistent-field method, implemented with a split graph unitary group approach,” *Journal of Physical Chemistry* **94**, 5477–5482 (1990).
- ⁷OpenMolcas Developers, “Openmolcas users’ guide: Rasscf,” <https://molcas.org/documentation/manual/>, accessed 2026-01-24.
- ⁸F. Aquilante, J. Autschbach, R. K. Carlson, *et al.*, “Modern quantum chemistry with OpenMolcas,” *Journal of Chemical Physics* **152**, 214117 (2020).
- ⁹O. Vahtras, J. Almlöf, and M. W. Feyereisen, “Integral approximations for lcao-scf calculations,” *Chemical Physics Letters* **213**, 514–518 (1993).
- ¹⁰F. Aquilante, T. B. Pedersen, A. Sanchez de Meras, and H. Koch, “Cholesky decomposition techniques in electronic structure theory,” *Journal of Chemical Physics* **127**, 114107 (2007).

¹¹Q. Sun, T. C. Berkelbach, N. S. Blunt, *et al.*, “Pyscf: the python-based simulations of chemistry framework,” *WIREs Computational Molecular Science* **8**, e1340 (2018).

¹²Q. Sun, X. Zhang, S. Banerjee, P. Bao, M. Barbry, N. S. Blunt, N. A. Bogdanov, G. H. Booth, J. Chen, Z.-H. Cui, *et al.*, “Recent developments in the pyscf program package,” *The Journal of chemical physics* **153** (2020).

¹³J. J. Bao, D. Zhang, S. Zhang, L. Gagliardi, and D. G. Truhlar, “A hybrid meta on-top functional for multiconfiguration pair-density functional theory,” *Proceedings of the National Academy of Sciences* **122**, e2419413121 (2025).

¹⁴H. Lischka, R. Shepard, F. B. Brown, *et al.*, “The COLUMBUS program system,” *WIREs Computational Molecular Science* **1**, 191–199 (2011).

¹⁵OpenAI, “[Introducing Codex](#),” (2025), accessed 2026-01-25.

¹⁶OpenAI, “[Chatgpt](https://chat.openai.com/),” <https://chat.openai.com/> (2025), large language model; model version GPT-5.2; accessed January 2026.

Appendix A: Pseudocode listings

1. DRT construction and CSF indexing

Algorithm A1: Construct DRT transition map χ and walk counts W

Input: Feasible nodes \mathcal{V} (or inferred from rules); local branching rules (occupancy/spin constraints).
Output: Transition map $\chi(v, d)$; walk counts $W(v)$; prefix sums $\Pi(v, d)$.

```

1: Enumerate feasible nodes layer-by-layer. Assign each node  $v \in \mathcal{V}$  an index.
2: For each node  $v$ , for each step  $d \in \mathcal{D}$ , set  $\chi(v, d)$  to the child node index or  $-1$  if infeasible.
3: Initialize walk counts at leaves:  $W(v) = 1$  if  $v$  is a valid terminal node, else 0.
4: for  $k = n_{\text{orb}} - 1$  down to 0 do
5:   for nodes  $v$  in layer  $k$  do
6:      $W(v) \leftarrow \sum_{d \in \mathcal{D}} W(\chi(v, d))$  (with  $W(-1) \equiv 0$ ).
7:   end for
8: end for
9: for each node  $v$  do
10:    $\Pi(v, E) \leftarrow 0$ .
11:   For  $d$  in order  $E < U < L < D$ , set
         $\Pi(v, d_{\text{next}}) \leftarrow \Pi(v, d) + W(\chi(v, d))$ .
12: end for
```

Algorithm A2: Unranking: compute CSF path from index j

Input: DRT transition map χ and prefix sums Π ; target index $j \in \{0, \dots, N_{\text{CSF}} - 1\}$.
Output: Step sequence $\mathbf{d}^{(j)} = (d_1, \dots, d_{n_{\text{orb}}})$ and node sequence $(v_0, \dots, v_{n_{\text{orb}}})$.

```

1:  $v_0 \leftarrow$  root node.
2: for  $k = 1$  to  $n_{\text{orb}}$  do
3:   Find unique step  $d \in \mathcal{D}$  such that
       $\Pi(v_{k-1}, d) \leq j < \Pi(v_{k-1}, d_{\text{next}})$ .
4:    $d_k \leftarrow d$ .
5:    $j \leftarrow j - \Pi(v_{k-1}, d)$ .
6:    $v_k \leftarrow \chi(v_{k-1}, d)$ .
7: end for
```

2. Segment factors and neighbor oracle

Algorithm A3: Precompute tables for constant-time evaluation of $S(\cdot)$

Input: $b_{\text{max}} = \max_{v \in \mathcal{V}} b(v)$.

Output: A finite case map $M(\kappa, \tilde{d}, d, \Delta b) \mapsto m$ and a table of segment factors $F[m, b]$.

```

1: Identify the finite set of local segment configurations  $(\kappa, \tilde{d}, d, \Delta b)$ .
2: Assign each configuration a unique case index  $m = M(\kappa, \tilde{d}, d, \Delta b)$ .
3: for each case  $m$  and each local spin label  $b \in \{0, \dots, b_{\text{max}}\}$  do
4:   Compute the corresponding segment factor  $F[m, b]$  using the standard closed-form rules.
5: end for
```

Algorithm A4: Segment-walk to enumerate nonzero $\langle \Phi_i | E_{pq} | \Phi_j \rangle$

Input: Ket path $(v_0^{(j)}, \mathbf{d}^{(j)})$, transition map χ , prefix sums Π , local factor evaluation $S(\cdot)$.
Output: Set of pairs (i, ω) such that $\omega = \langle \Phi_i | E_{pq} | \Phi_j \rangle \neq 0$.

```

1: Determine segment boundaries  $p_< = \min(p, q)$  and  $p_> = \max(p, q)$ .
2: Determine boundary nodes  $v_{p_<}^{(j)}$  and  $v_{p_>+1}^{(j)}$  on ket path.
3: Initialize a worklist with the boundary condition at layer  $p_<$ .
4: while worklist not empty do
5:   Pop a partial bra walk (current node  $u_k$ , partial factor  $\omega$ ).
6:   if  $k > p_>$  then
7:     Complete remaining steps to form full bra index  $i$  via ranking with  $\Pi$ .
8:     Emit  $(i, \omega)$ .
9:   else
10:    for all feasible step substitutions consistent with  $(p, q)$  and segment rules do
11:      Propose next node  $u_{k+1} = \chi(u_k, \tilde{d})$ .
12:      Update factor  $\omega \leftarrow \omega \cdot S(\cdot)$ .
13:      Push updated partial walk to worklist.
14:    end for
15:  end if
16: end while

```

3. Operator-direct matvec and Davidson

Algorithm A5: Operator-direct $\sigma = Hc$ using a segment-walk neighbor oracle

Input: Coefficients $c \in \mathbb{R}^{N_{\text{CSF}}}$; effective one-electron integrals h_{pq}^{eff} ; two-electron backend either dense $\mathbf{V}^{(2e)}$ or DF/Cholesky \mathbf{B} .

Output: Output vector $\sigma \in \mathbb{R}^{N_{\text{CSF}}}$.

```

1: Initialize  $\sigma \leftarrow \mathbf{0}$ .                                ▷ One-electron part
2: for  $j = 0$  to  $N_{\text{CSF}} - 1$  do
3:    $\sigma_j += c_j \sum_p h_{pp}^{\text{eff}} n_p(\Phi_j)$ .
4:   for all feasible particle/hole pairs  $(p, q) \in \mathcal{P}(j) \times \mathcal{H}(j)$  do
5:     Use Algorithm A4 to enumerate  $(i, \Omega_{ij}^{(pq)})$ .
6:     for each output  $(i, \Omega)$  do
7:        $\sigma_i += c_j h_{pq}^{\text{eff}} \Omega$ .
8:     end for
9:   end for
10: end for ▷ Two-electron part (intermediate weights) ▷ Enumerate sparse intermediate couplings  $C_{\mu j}^{(rs)}$  and
      assemble pair-space vectors  $\mathbf{C}^{(\mu j)}$ 
11: for  $j = 0$  to  $N_{\text{CSF}} - 1$  do
12:   for all feasible pairs  $(r, s) \in \mathcal{P}(j) \times \mathcal{H}(j)$  do
13:     Use Algorithm A4 to enumerate  $(\mu, \Omega_{\mu j}^{(rs)})$ .
14:     for each output  $(\mu, \Omega)$  do
15:       Accumulate  $C_{\mu j}^{(rs)} \leftarrow \Omega$  into the pair-space vector  $\mathbf{C}^{(\mu j)}$ .
16:     end for
17:   end for
18: end for                                              ▷ Contract with integrals to form weights  $g_{pq}^{(\mu j)}$ 
19: Compute weights  $\mathbf{g}^{(\mu j)}$  for all tasks using either dense or DF/Cholesky backend.
20: for each task  $(\mu, j)$  do
21:   for each nonzero pair  $(p, q)$  in  $\mathbf{g}^{(\mu j)}$  do
22:     Use Algorithm A4 to enumerate  $(i, \Omega_{i\mu}^{(pq)})$ .
23:     for each output  $(i, \Omega)$  do
24:        $\sigma_i += c_j g_{pq}^{(\mu j)} \Omega$ .
25:     end for
26:   end for
27: end for

```

Algorithm A6: Davidson eigensolver with operator-direct matvec

Input: Matvec routine $\mathbf{y} \leftarrow \mathbf{Hx}$ (Algorithm A5); diagonal H_{diag} ; number of roots n_{root} ; tolerance ε ; maximum subspace size m_{max} .

Output: Approximate eigenpairs $(E^{(n)}, \mathbf{c}^{(n)})$ for $n = 1, \dots, n_{\text{root}}$.

```

1: Initialize orthonormal subspace  $\mathbf{V}$  (e.g., guess vectors).
2: while not converged do
3:   Apply matvec to form  $\mathbf{W} = \mathbf{HV}$ .
4:   Form projected matrix  $\mathbf{H}_{\text{sub}} = \mathbf{V}^T \mathbf{W}$ .
5:   Solve  $\mathbf{H}_{\text{sub}} \mathbf{U} = \mathbf{U} \Lambda$  for lowest  $n_{\text{root}}$  eigenpairs.
6:   Form Ritz vectors  $\mathbf{X} = \mathbf{VU}$  and residuals  $\mathbf{R} = \mathbf{WU} - \mathbf{X} \Lambda$ .
7:   if all  $\|\mathbf{r}^{(n)}\| < \varepsilon$  then
8:     Converged.
9:   else
10:    Precondition residuals using diagonal  $H_{\text{diag}}$  and expand subspace.
11:    Orthonormalize and, if  $\dim(\mathbf{V}) > m_{\text{max}}$ , restart.
12:   end if
13: end while

```

4. GPU workflow**Algorithm A7: GPU count–scan–write for batched segment-walk enumeration**

Input: A set of work items $\{\omega_t\}_{t=1}^{N_{\text{work}}}$, where $\omega_t = (p_t, q_t, j_t)$; DRT tables χ, Π ; ket paths $\mathbf{d}^{(j)}$; segment-factor tables from Algorithm A3.

Output: Flat arrays of outputs $(I[\ell], \Omega[\ell])$ such that each work item t writes a contiguous segment.

```

1: Count kernel (custom CUDA): for each work item  $t$  in parallel, run a counting-only variant of Algorithm A4
   to compute  $n_t = |\mathcal{O}(p_t, q_t; j_t)|$ .
2: Exclusive scan: compute offsets  $o_t = \sum_{t' < t} n_{t'}$  and total  $N_{\text{out}} = \sum_t n_t$ .
3: Allocate (or reuse) output buffers  $I[0:N_{\text{out}}]$  and  $\Omega[0:N_{\text{out}}]$ .
4: Write kernel (custom CUDA): for each work item  $t$  in parallel, rerun Algorithm A4 and write its outputs
   to indices  $\ell \in [o_t, o_t + n_t]$ .

```